Nucleon Electromagnetic Form Factors from Lattice QCD

Yong-Chull Jang

Physics Department, Brookhaven National Laboratory

(PNDME Collaboration)

2019 Lattice Workshop for US – Japan Intensity Frontier Incubation
March 25 – 27, 2019

Nucleon Structure, Proton Radius

- $e - p$ scattering, H laser spectroscopy $r_{E,p} = 0.875(6)\,\mathrm{fm}$
  [CODATA2014 RMP **88**, 035009 (2016)]
- muonic hydrogen laser spectroscopy $r_{E,p} = 0.8409(4)\,\mathrm{fm}$
  [R. Pohl *et.al.*, Nature **466**, 213 (2010)]
  [A. Antognini *et al.*, Science **339**, 417 (2013)]
- Lattice QCD
- New Physics (?)

Form Factor Decomposition

EM form factors, charge, magnetic moment, charge radii :

$$\langle N(\vec{p}_f)|V_\mu(\vec{q})|N(\vec{p}_i)\rangle = \overline{u}(\vec{p}_f)\left[F_1(Q^2)\gamma_\mu + \sigma_{\mu\nu}q_\nu\frac{F_2(Q^2)}{2M}\right]u(\vec{p}_i)$$

$$q = p_f - p_i,\ Q^2 = -q^2 = \vec{p}_f^2 - (E-M)^2,\ \vec{p}_i = 0$$

$$G_E(Q^2) = F_1(Q^2) - \frac{Q^2}{4M^2}F_2(Q^2) \to \langle r_E^2\rangle,\ G_E(0) \equiv g_V$$

$$G_M(Q^2) = F_1(Q^2) + F_2(Q^2) \qquad \to \langle r_M^2\rangle,\ G_M(0)/g_V \equiv \mu$$

$$\langle r_{E,M}^2\rangle = -6\frac{d}{dQ^2}\left(\frac{G_{E,M}(Q^2)}{G_{E,M}(0)}\right)\Bigg|_{Q^2=0}$$

$$\mu^p = 1 + \kappa^p,\ \kappa^p = 1.7928$$

$$\mu^n = \kappa^n = -1.9130$$

Isospin Symmetry

- *Isovector* current $V_\mu^{u-d} = \bar{u}\gamma_\mu u - \bar{d}\gamma_\mu d$ on the lattice

$$\langle p|V_\mu^{u-d}|p\rangle = \langle p|V_\mu^{\text{em}}|p\rangle - \langle n|V_\mu^{\text{em}}|n\rangle$$

$$V_\mu^{\text{em}} = \frac{2}{3}\bar{u}\gamma_\mu u - \frac{1}{3}\bar{d}\gamma_\mu d$$

Lattice Methodology

Ensemble ID	a (fm)	M_π^{sea} (MeV)	M_π^{val} (MeV)	$L^3 \times T$	$M_\pi^{\text{val}} L$	τ/a	N_{conf}	$N_{\text{meas}}^{\text{HP}}$	$N_{\text{meas}}^{\text{LP}}$
a15m310	0.1510(20)	306.9(5)	320(5)	$16^3 \times 48$	3.93	$\{5, 6, 7, 8, 9\}$	1917	7668	122,688
a12m310	0.1207(11)	305.3(4)	310.2(2.8)	$24^3 \times 64$	4.55	$\{8, 10, 12\}$	1013	8104	64,832
a12m220S	0.1202(12)	218.1(4)	225.0(2.3)	$24^3 \times 64$	3.29	$\{8, 10, 12\}$	946	3784	60,544
a12m220	0.1184(10)	216.9(2)	227.9(1.9)	$32^3 \times 64$	4.38	$\{8, 10, 12\}$	744	2976	47,616
a12m220L	0.1189(09)	217.0(2)	227.6(1.7)	$40^3 \times 64$	5.49	$\{8, 10, 12, 14\}$	1000	4000	128,000
a09m310	0.0888(08)	312.7(6)	313.0(2.8)	$32^3 \times 96$	4.51	$\{10, 12, 14, 16\}$	2263	9052	144,832
a09m220	0.0872(07)	220.3(2)	225.9(1.8)	$48^3 \times 96$	4.79	$\{10, 12, 14, 16\}$	964	7712	123,392
a09m130W	0.0871(06)	128.2(1)	138.1(1.0)	$64^3 \times 96$	3.90	$\{8, 10, 12, 14, 16\}$	1290	5160	165,120
a06m310	0.0582(04)	319.3(5)	319.6(2.2)	$48^3 \times 144$	4.52	$\{16, 20, 22, 24\}$	1000	8000	64,000
a06m310W						$\{18, 20, 22, 24\}$	500	2000	64,000
a06m220	0.0578(04)	229.2(4)	235.2(1.7)	$64^3 \times 144$	4.41	$\{16, 20, 22, 24\}$	650	2600	41,600
a06m220W						$\{18, 20, 22, 24\}$	649	2596	41,536
a06m135	0.0570(01)	135.5(2)	135.6(1.4)	$96^3 \times 192$	3.7	$\{16, 18, 20, 22\}$	675	2700	43,200

- Clover valence quarks on the HISQ Ensembles $N_f = 2 + 1 + 1$
- smearing with larger gaussian width W
- different volumes for the same pion mass and lattice spacing
- High statistics data at $a = 0.09$ fm
- Truncated solver bias correction for all τ/a

Controlling Excited States: multistates fits

$$C^{2\text{pt}}(t, \boldsymbol{p}) = |\mathcal{A}_0|^2 e^{-E_0 t} + |\mathcal{A}_1|^2 e^{-E_1 t} + |\mathcal{A}_2|^2 e^{-E_2 t} + |\mathcal{A}_3|^2 e^{-E_3 t} + \cdots$$

- 2-state fit $\rightarrow$ 4-state fit
- The lowest three states Energies and $\mathcal{A}$mplitudes are feed into 3-pt correlator analysis.
- plot effective mass from fits and data $E_{\text{eff}}(t) = \log \dfrac{C^{2\text{pt}}(t)}{C^{2\text{pt}}(t+1)} \rightarrow E_0$

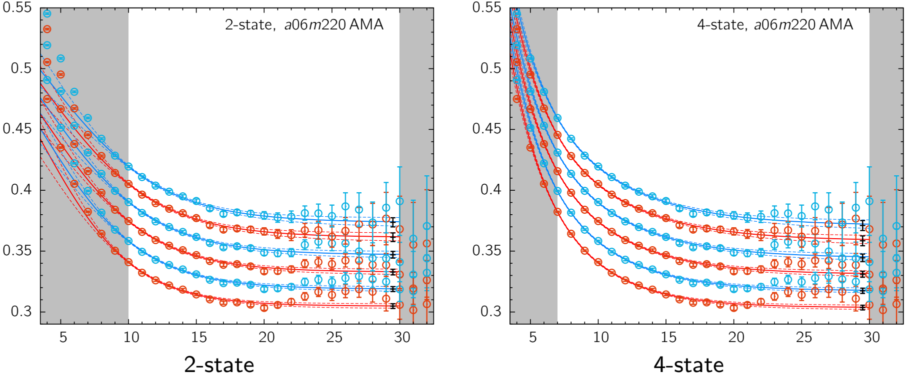

Controlling Excited States: different smearing size

- Covariant gaussian smearing: $\left[1 + \sigma^2 \nabla^2 / (4N)\right]^N$
- 4-state fit, $\boldsymbol{p} = 0$

$$C^{2\text{pt}}(t, \boldsymbol{p}) = |\mathcal{A}_0|^2 e^{-M_0 t} + |\mathcal{A}_1|^2 e^{-M_1 t} + |\mathcal{A}_2|^2 e^{-M_2 t} + |\mathcal{A}_3|^2 e^{-M_3 t} + \cdots$$

- Larger size of smearing radius improves an overlap with the ground state
  $\rightarrow$ plateau appears from earlier t
- At large t, the correlator become noisier

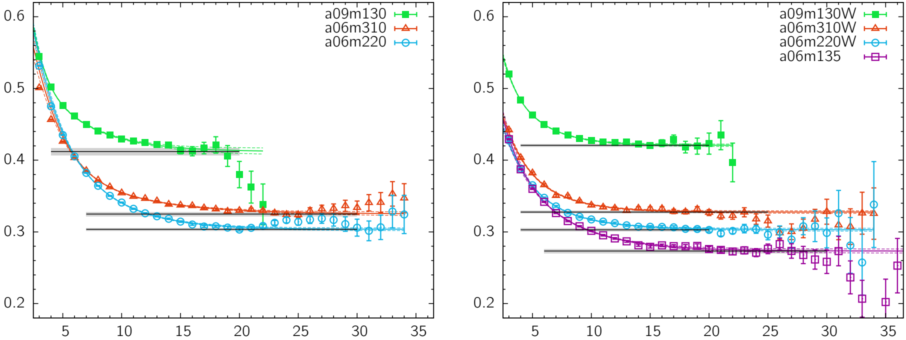

$\sigma = 5.5, 6.5, 5.5$ $\qquad$ $\sigma = 7, 12, 11, 9$

Extracting Form Factors from 3-pt Correlaotrs

- Matrix elements $\langle m'|\mathcal{O}_\Gamma|n\rangle$ are extracted from a simultaneous fit to the correlator $C_\Gamma^{(3\text{pt})}$ calculated at multiple source and sink separation τ.

$$\begin{aligned}
C_\Gamma^{(3\text{pt})}(t;\tau;\boldsymbol{p}',\boldsymbol{p}=\boldsymbol{0}) = {} & |\mathcal{A}_0'||\mathcal{A}_0|\langle 0'|\mathcal{O}_\Gamma|0\rangle e^{-E_0 t - M_0(\tau - t)} \\
& + |\mathcal{A}_1'||\mathcal{A}_1|\langle 1'|\mathcal{O}_\Gamma|1\rangle e^{-E_1 t - M_1(\tau - t)} + |\mathcal{A}_2'||\mathcal{A}_2|\langle 2'|\mathcal{O}_\Gamma|2\rangle e^{-E_2 t - M_2(\tau - t)} \\
& + |\mathcal{A}_0'||\mathcal{A}_1|\langle 0'|\mathcal{O}_\Gamma|1\rangle e^{-E_0 t - M_1(\tau - t)} + |\mathcal{A}_1'||\mathcal{A}_0|\langle 1'|\mathcal{O}_\Gamma|0\rangle e^{-E_1 t - M_0(\tau - t)} \\
& + |\mathcal{A}_0'||\mathcal{A}_2|\langle 0'|\mathcal{O}_\Gamma|2\rangle e^{-E_0 t - M_2(\tau - t)} + |\mathcal{A}_2'||\mathcal{A}_0|\langle 2'|\mathcal{O}_\Gamma|0\rangle e^{-E_2 t - M_0(\tau - t)} \\
& + |\mathcal{A}_1'||\mathcal{A}_2|\langle 1'|\mathcal{O}_\Gamma|2\rangle e^{-E_1 t - M_2(\tau - t)} + |\mathcal{A}_2'||\mathcal{A}_1|\langle 2'|\mathcal{O}_\Gamma|1\rangle e^{-E_2 t - M_1(\tau - t)} + \cdots
\end{aligned}$$

- $\langle 2'|\mathcal{O}_\Gamma|2\rangle = 0$

- Decompose the ground state matrix elements

$$\langle 0'|\mathcal{O}_\Gamma|0\rangle = K_{E,\Gamma} G_E(Q^2) + K_{M,\Gamma} G_M(Q^2)$$

- Data is displayed using the following ratio.

$$\mathcal{R}_\Gamma(t,\tau,\boldsymbol{p}',\boldsymbol{p}) = \frac{C_\Gamma^{(3\text{pt})}(t,\tau;\boldsymbol{p}',\boldsymbol{p})}{C^{(2\text{pt})}(\tau,\boldsymbol{p})} \times \left[\frac{C^{(2\text{pt})}(t,\boldsymbol{p})C^{(2\text{pt})}(\tau,\boldsymbol{p})C^{(2\text{pt})}(\tau - t,\boldsymbol{p}')}{C^{(2\text{pt})}(t,\boldsymbol{p}')C^{(2\text{pt})}(\tau,\boldsymbol{p}')C^{(2\text{pt})}(\tau - t,\boldsymbol{p})}\right]^{1/2} \underset{\substack{\tau\to\infty \\ 0\ll t,\tau - t}}{\longrightarrow} \langle 0'|\mathcal{O}_\Gamma|0\rangle$$

Extraction of G_E

- $\mathrm{Im}\, C(V_i) \to K q_i G_E$, $K = 1/\sqrt{2E(E+M)}$
- $\mathrm{Re}\, C(V_4) \to K(E+M) G_E$
- Two channels result in different G_E mostly for $Q^2 \lesssim 0.2$.

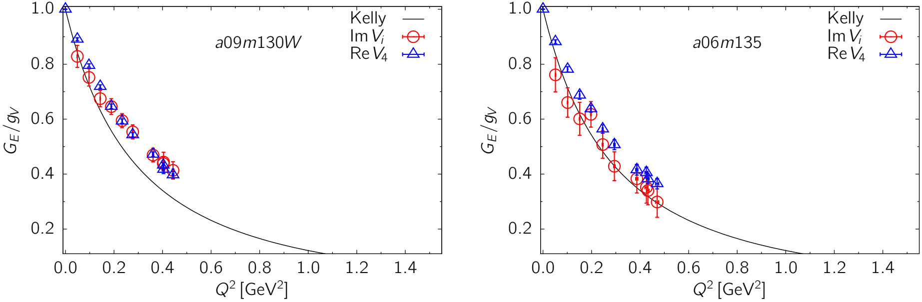

- Excited states contaminations to the two channels are very different.
- $G_E(0)$ is not accessible to V_i.

Extraction of G_E

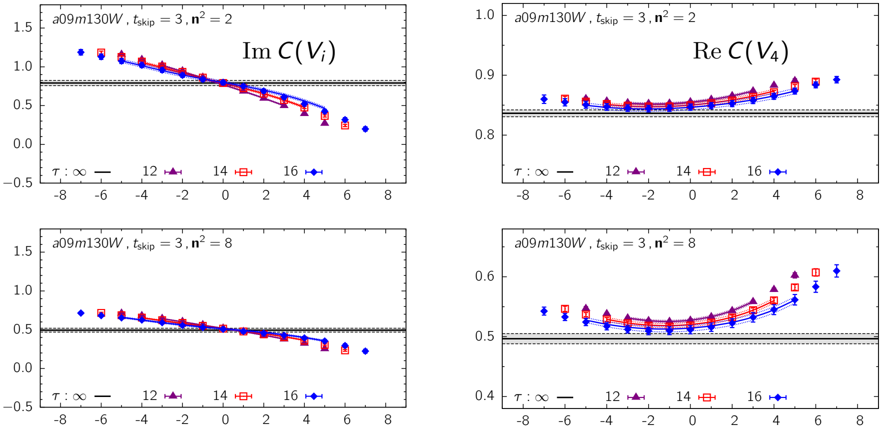

- Excited states contaminations to $\mathrm{Im}\, C(V_i)$ and $\mathrm{Re}\, C(V_4)$ are very different.
- $G_E(0)$ is not accessible to V_i.
- We use G_E from $\mathrm{Re}\, C(V_4)$.

Extraction of G_E

- $\mathrm{Re}\, C(V_4)$ converges from above: overestimates the G_E ?
- G_E/g_V versus Q^2/M_N^2: all 13 ensemble data falls into a thin band.
- Comparison to the experimental data is made with the Kelly parameterization.

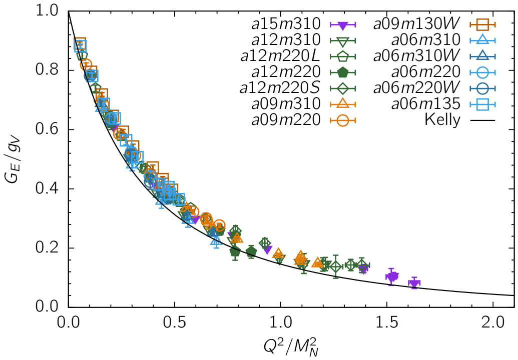

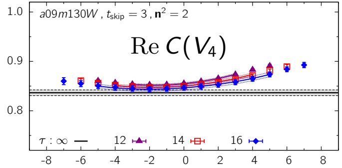

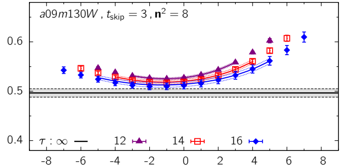

Extraction of G_M

- $\mathrm{Re}\, C(V_i) \to -K\epsilon_{ij3} q_j G_M, \;\; K = 1/\sqrt{2E(E+M)}$
- Example of the excited states effect: $a06m135 \Rightarrow$
- For the small Q^2 ($\boldsymbol{n}^2 = 1, 2$), the convergence is from below: underestimates the G_M ?
  Or, a large finite volume effect at small Q^2 ?
  [B. C. Tiburzi, PRD **77**, 014510 (2008)]

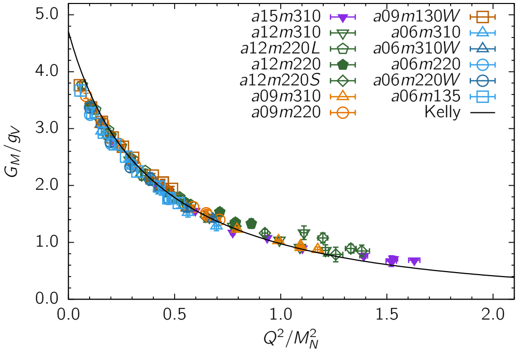

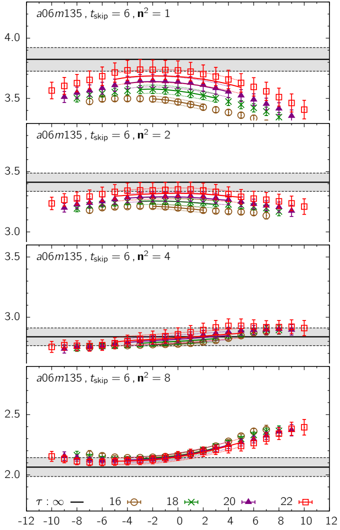

Estimate of $G_M(Q^2 = 0)$

- G_M/G_E (or G_E/G_M) for $Q^2 \lesssim 0.6\mathrm{GeV}^2$ is approximately linear in Q^2.
- $G_M(0)$: a linear fit to G_M/G_E incluing 6 (or 5 when data lacks) low Q^2 point is extrapolated to $Q^2 = 0$.
- The derived data points stabilizes the Q^2 fit, and thus extraction of charge radius r_M.

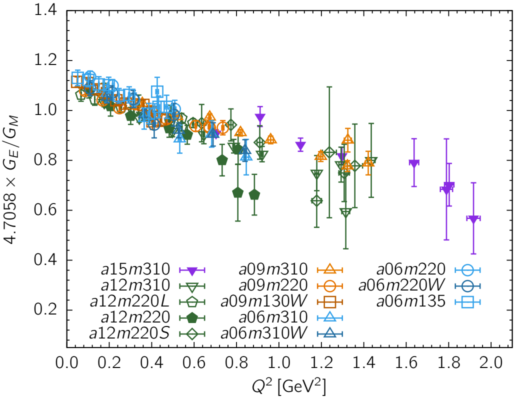

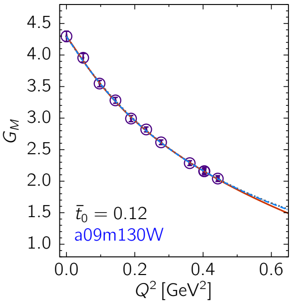

($\mu_{\mathrm{phys}}^{p-n} = 4.7058$)

Form Factor Q^2 Parameterization

- Dipole

$$G_E(Q^2) = \frac{G_E(0)}{(1+Q^2/\mathcal{M}_E^2)^2} \quad \Longrightarrow \quad \langle r_E^2 \rangle = \frac{12}{\mathcal{M}_E^2}$$

- z-expansion

$$G_E(Q^2) = \sum_{k=0}^{\infty} a_k z(Q^2)^k \,, \; z = \frac{\sqrt{t_{\rm cut}+Q^2} - \sqrt{t_{\rm cut}+\bar{t}_0}}{\sqrt{t_{\rm cut}+Q^2} + \sqrt{t_{\rm cut}+\bar{t}_0}} \,, \; (t_{\rm cut} = 4M_\pi^2)$$

- Weak unitarity constraint: a_k are bounded and decreasing at sufficiently large k

$$\sum_{k=n} a_k^2 < \infty$$

We impose a prior $|a_k| < 5$ for G_E and $G_M/5$. crucial to see a convergence

- Sum rules implement $Q^n G_E(Q^2) \to 0$ for $n = 0, 1, 2, 3$: $\mathcal{O}(1/k^4)$ fall-off of a_k strong constraint

$$\sum_{k=0}^{k_{\rm max}} a_k = 0 \,, \quad \sum_{k=n}^{k_{\rm max}} k(k-1)\ldots(k-n+1) a_k = 0 \quad (n = 1, 2, 3)$$

z-expansion: Experimental Data

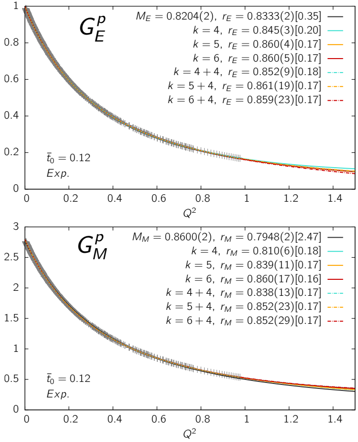

[rebinned experimental data, D. Higinbotham]

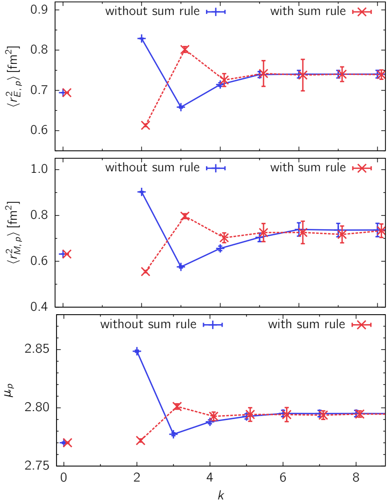

- z-expansion converges for $k \geq 5$
- fits with/without sum rules converges to the same value

z-expansion: Lattice Data

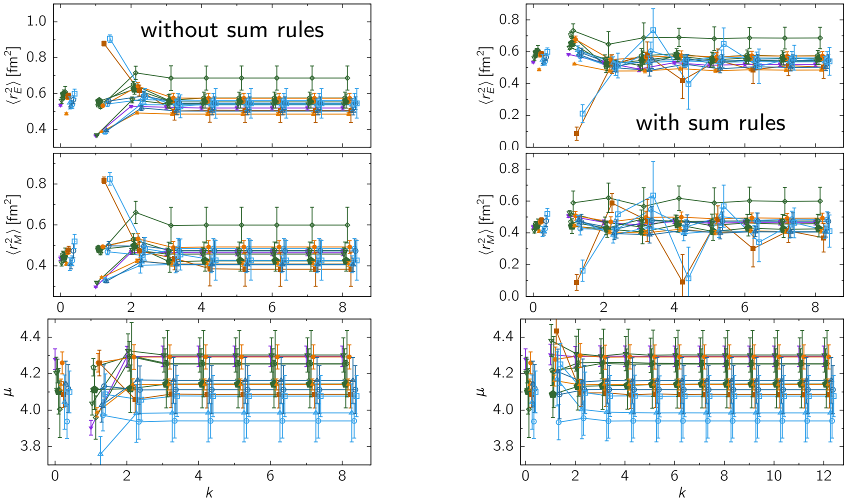

- $k = 0$: dipole fit
- Fits with the sum rules slowly converges. But, later it converges to the same value to the fit without the sum rules. Avoiding overfitting, we take z^{4+0} fit.

- with a cutoff $Q^2 \sim 1\mathrm{GeV}^2$, we drop the data points with large discretization error.

- $|z| \lesssim 0.2$

  $\bar{t}_0 \in \{0.12, 0.2, 0.4\}$

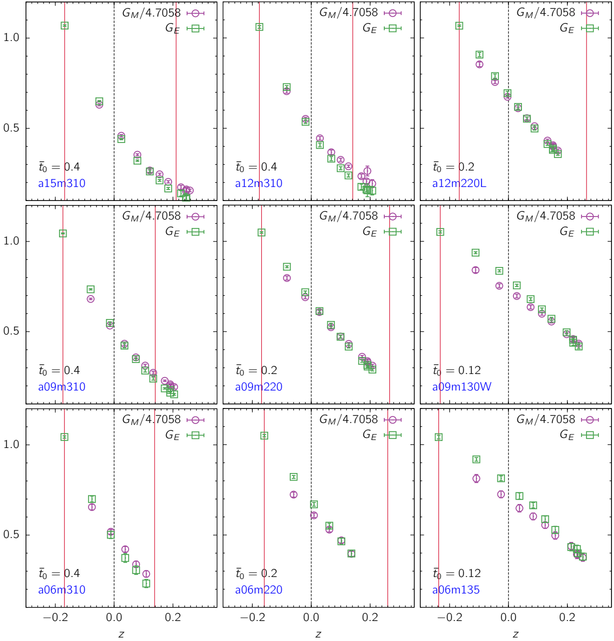

r_E^2: Chiral, Continuum, Finite Volume (CCFV) Extrapolation

$$\langle r_E^2 \rangle = c_1^E + c_2^E a + c_3^E \ln(M_\pi^2/M_\rho^2) + c_4^E \ln(M_\pi^2/M_\rho^2) e^{-M_\pi L}$$

$$dipole : 0.586(17)(?)\,\mathrm{fm}^2 \qquad z^4 : 0.591(41)(?)\,\mathrm{fm}^2$$

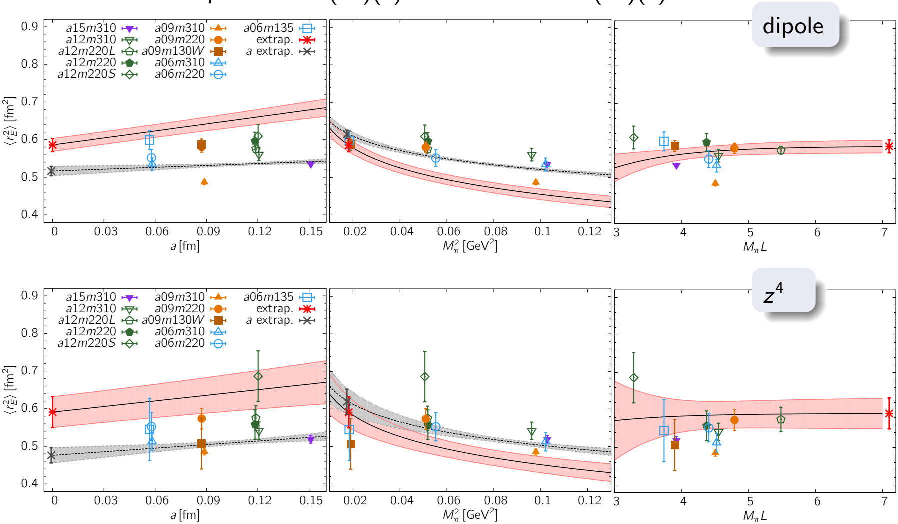

G_E: Lattice Spacing and Pion Mass Dependences

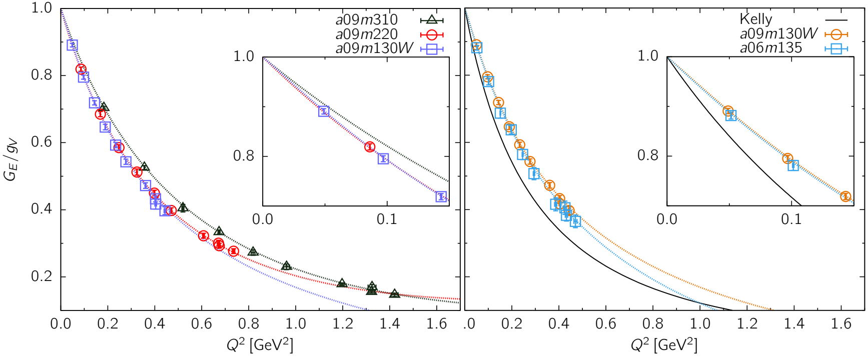

- Q^2 fit to $a09m130W$ follows $a09m220$ for $0.05 < Q^2 0.4\,\mathrm{GeV}^2$. But as it approaches to $Q^2 = 0$ the slope of $a09m130W$ intercepts between $a09m220$ and $a09m310$.
- r_E^2 is slightly larger for $a06m135$, $0.545(83)\,\mathrm{fm}^2$, than $a09m130W$, $0.507(67)\,\mathrm{fm}^2$. It is not easy to see a resolution from the fit curve (z^4). Factor 6 inflation of $G_E'(0)$.
- Thus, the data points at the smaller Q^2 can change the results.
- Lattice data is more linear in Q^2 than the Kelly curve.

r_M^2: Chiral, Continuum, Finite Volume (CCFV) Extrapolation

$$\langle r_M^2 \rangle = c_1^M + c_2^M a + c_3^M / M_\pi + (c_4^M / M_\pi) e^{-M_\pi L}$$

$$dipole : 0.495(29)(?)\,\mathrm{fm}^2 \qquad z^4 : 0.450(65)(?)\,\mathrm{fm}^2$$

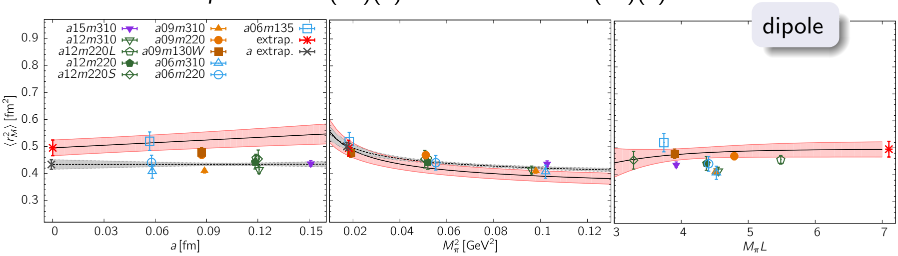

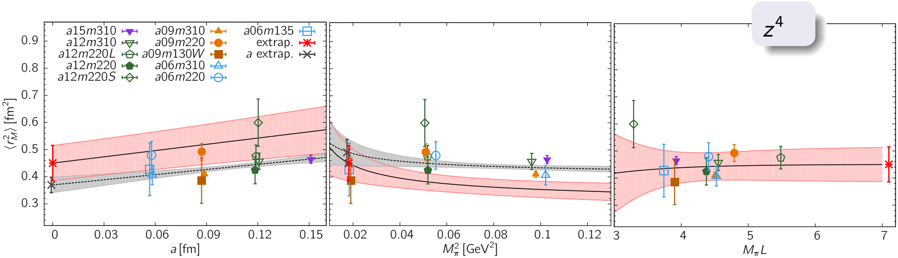

$\mu_p - \mu_n$: Chiral, Continuum, Finite Volume (CCFV) Extrapolation

$$\langle \mu \rangle = c_1^\mu + c_2^\mu a + c_3^\mu M_\pi + c_4^\mu M_\pi \left(1 - \frac{2}{M_\pi L}\right) e^{-M_\pi L}$$

dipole : 3.975(84)(?) z^4 : 3.939(86)(?)

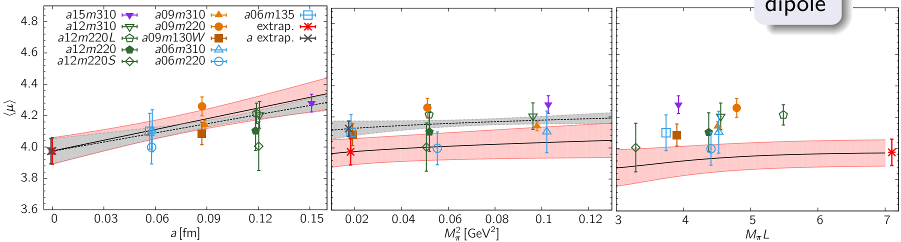

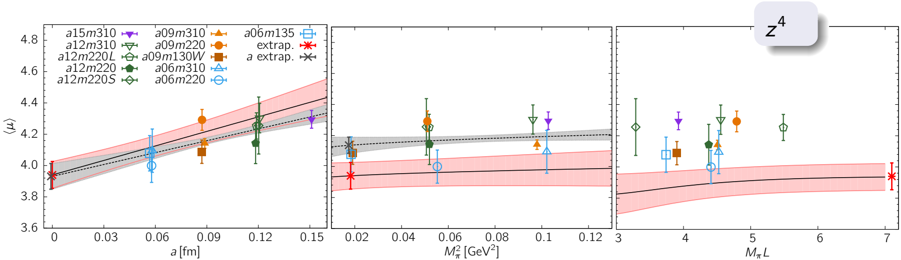

G_M: Lattice Spacing and Pion Mass Dependences

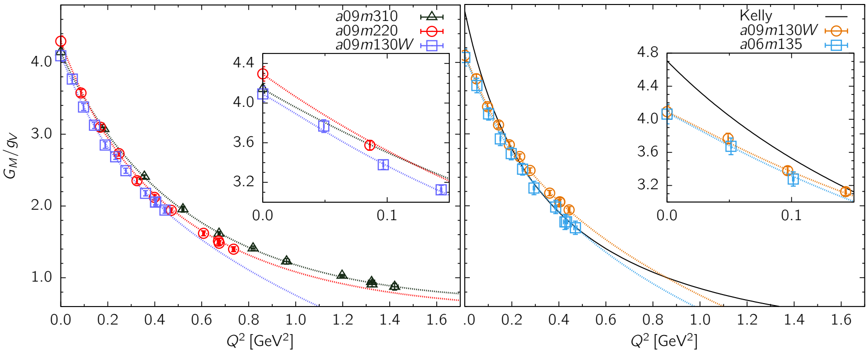

- The slope at $Q^2 = 0$ does not show a monotone behavior as our leading order term $1/M_\pi$.
- The smallest available $Q^2 \sim 0.2\,\mathrm{GeV}^2$ for $a09m310$ is large compared with $a09m220$ and $a09m130W$.
- Lattice data is more linear in Q^2 than the Kelly curve.

Comparison with Other Near Physical Pion Mass Calculations

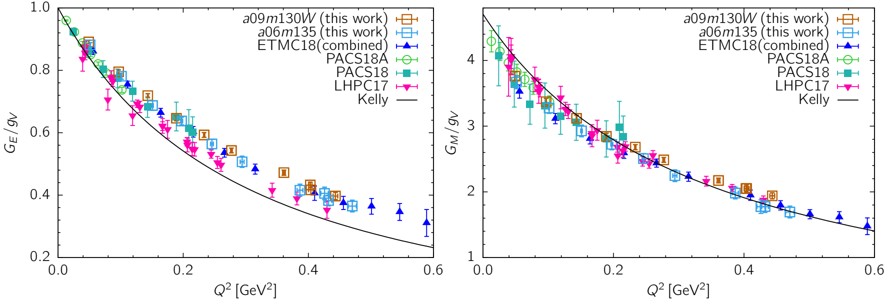

- For $Q^2 < 0.2\,\mathrm{GeV}^2$, G_E (G_M) from lattice calculations approaches the Kelly parameterization of experimental data from above (below).
- PACS'18 and LHPC'17 data are consistent with the rest, but the errors are larger.
- All the PACS'18A data are at $Q^2 < 0.1\,\mathrm{GeV}^2$ and show better agreement with the Kelly curve.

Comparison with Other Near Physical Pion Mass Calculations

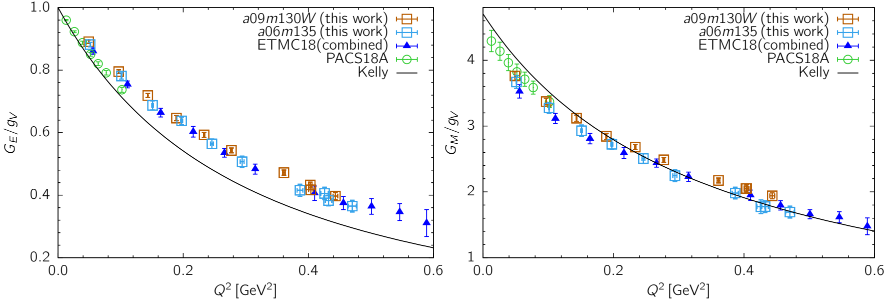

	a [fm]	M_π [MeV]	$L^3 \times T$	$M_\pi^{\rm val} L$	τ/a	$N_{\rm conf}$	$N_{\rm meas}$	Action
*a*09*m*130*W*	0.0871(6)	138.1(1.0)	$64^3 \times 96$	3.90	$\{8, 10, 12, 14, 16\}$	1290	165,120	2+1+1 HISQ
*a*06*m*135	0.0570(1)	135.6(1.4)	$96^3 \times 192$	3.7	$\{16, 18, 20, 22\}$	675	43,200	+ Clover
ETMC'18	0.0809(4)	138(1)	$64^3 \times 128$	3.62	$\{12, 14, 16, 18, 20\}$	750	3K–48K	2+1+1 TM
ETMC'18	0.0938(3)	130(2)	$64^3 \times 128$	3.97	$\{12, 14, 16\}$	330–1040	5K–17K	2 TM
PACS'18A	0.0846(7)	146	$96^3 \times 96$	6.01	$\{15\}$	200	12,800	2+1 Clover
PACS'18	0.0846(7)	135	$128^3 \times 128$	7.41	$\{10, 12, 14, 16\}$	20	2.5K–10K	2+1 Clover
LHPC'17	0.093	135	$64^3 \times 64$	4.08	$\{10, 13, 16\}$	442	56,576	2+1 Clover

- All the PACS'18A data are at $Q^2 < 0.1\,\mathrm{GeV}^2$ and show better agreement with the Kelly curve. Further calculations with multiple lattice spacings, larger Q^2 points, higher statistics are interesting.

Summary

- We analyzed 11 ensembles of $2+1+1$-flavor HISQ sea quarks with clover valence quark. ($a \approx 0.06, 0.09, 0.12, 0.15\,\mathrm{fm}$, $M_\pi \approx 135, 220, 310\,\mathrm{MeV}$, $3.3 \lesssim M_\pi L \lesssim 5.5$)
- 13 calculations of G_E and G_M have small variations in a and M_π.
- With high statistics of $\mathcal{O}(10^5)$, z-expansion at different truncations and constraints became more consistent.
- The weak unitarity constraint helps to stabilize the z-expansion.
- z-expansion results are consistent with the dipole fit, but the errors are 2–3 times larger.
- Smaller Q^2 data points are highly desirable in future calculations.

- Two physical pion mass ensembles at $a = 0.09, 0.06\,\mathrm{fm}$ anchor the chiral fit.
- Magnetic moment μ shows a significant a dependence, and it pushes the extrapolation results below the physical pion mass calculations.
- The extraction of r_E^2, r_M^2, μ could have $\mathcal{O}(10\%)$ errors due to each (1) statistics and ESC, and (2) parameterization of Q^2 behavior.
- We do not consider the smaller values of r_E^2, r_M^2, μ implies a significant deviations from the experimental values.

Thank you for your attention.